Supporting Information

Interlayer Registry Dictates Interfacial 2D Material Ferroelectricity

Wei Cao, Oded Hod*, and Michael Urbakh

Department of Physical Chemistry, School of Chemistry, The Raymond and Beverly Sackler Faculty of Exact Sciences and The Sackler Center for Computational Molecular and Materials Science, Tel Aviv University, Tel Aviv 6997801, Israel

*E-mail: odedhod@tauex.tau.ac.il

In this supplementary information, we provide additional details on certain aspects of the study reported in the manuscript. The following issues are discussed:

1. Interlayer Polarization Registry Index of Bilayer h-BN

1.1 Density functional theory computational details

The initial structure of the h-BN bilayer was constructed from two relaxed monolayers (with a lattice constant of $a = 2.51\,\text{Å}$) stacked at the AB configuration with an interlayer distance of $h_0 = 3.352\,\text{Å}$. Bilayer geometry optimization was then performed using the Broyden–Fletcher–Goldfarb–Shanno (BFGS) algorithm[1] with a force threshold of 1×10^{-5} Ry/bohr. The coordinates of the relaxed AB stacked h-BN bilayer are given at the end of this supplementary document. Polarization calculations were performed for vertically flexible shifted bilayer configurations of a parallelly stacked h-BN bilayer, where for each shift, the optimization allowed for relaxation of the vertical atomic positions with fixed lateral coordinates.

Geometry relaxation and out-of-plane polarization of the h-BN bilayer at various stacking modes was calculated via density functional theory using the plane-wave pseudopotential Quantum Espresso (QE) package.[2] The Perdew-Burke-Ernzerhof (PBE) generalized gradient exchange correlation functional was used along with the scalar-relativistic projector augmented wave (PAW) description of the core electrons.[3] Van der Waals (vdW) interlayer interactions were evaluated using the Grimme-D3 dispersion correction with Becke-Johnson (BJ) damping.[4, 5] The plane wave cutoff energy was set to 60 Ry with a k-mesh of 12×12×1 points using the Monkhorst-pack[6] scheme. A vacuum size of 10 nm along the normal direction was used to avoid interactions between adjacent bilayer images. To evaluate the vertical polarization of the system, the dipole correction was implemented and the resulting difference between the electrostatic potential values obtained above the top and below the bottom surfaces was calculated.

To verify the suitability of the PBE density functional approximation, we performed an additional single-point polarization calculation of the PBE optimized AB stacked h-BN bilayer, using the Heyd-Scuseria-Ernzerhof (HSE)[7-10] screened-exchange hybrid density functional. The minor differences in the electrostatic potential drop obtained using the two approximations (97 meV for HSE versus 103 meV for PBE) and their agreement with recent experimental measurements(109 meV)[11] indicate the suitability of the PBE approximation for the polarization calculations.

1.2 Global polarization registry index parameterization

The global polarization registry index for h-BN ($GPRI^{h-BN}$) was calculated via equations (1)-(2) of the main text. The Gaussian width parameterization was performed against a set of ground state laterally periodic DFT calculations (see supporting information (SI) section 1.1 above) of the relevant bilayer at different interlayer stackings, obtained by a relative interlayer shift along the armchair direction in steps of 0.1 Å. The fitting was performed by scanning all Gaussian width

parameters with a step of $0.01a/\sqrt{3}$ (a being the interlayer lattice constant of the relevant material) in the range 0.0 - $0.5\,a/\sqrt{3}$. For each set of parameters, the average difference between the $GPRI^{h-BN}$ and normalized DFT predictions along the sliding path was recorded. The parameters producing the minimal average difference along the entire path were chosen as the optimal set. Table S1 presents the corresponding Gaussian widths and the average differences between the reference DFT values and the $GPRI^{h-BN}$ results obtained using the optimal parameter set and the corresponding standard deviation.

Table S1. Fitted $GPRI^{h-BN}$ parameters for bilayer h-BN. The effective Gaussian width of each atomic pair appearing in the table is given in units of $a/\sqrt{3}$, where a is the lattice constant ($a_{h-BN} =$ 2.51 Å). Average ($\bar{x}$) difference between the normalized reference DFT potential drop profile and the $GPRI^{h-BN}$ results and the corresponding standard deviation (σ) obtained using the optimal parameter sets are provided.

h-BN	Parameter
$\sigma_B^N(\sigma_N^B)$	0.22
$\bar{x}$	0.0094
σ	0.0103

The polarization profiles calculated for rigid (using an interlayer distance of 3.35 Å) and vertically flexible shifts along the armchair h-BN direction are compared in Fig. S1. The figure demonstrates that vertical geometry relaxation has minor (less than 6%) influence on the bilayer polarization and that the PRI captures well both profiles. Notably, this demonstrates that PRI calculations using rigid model systems provide valuable predictions.
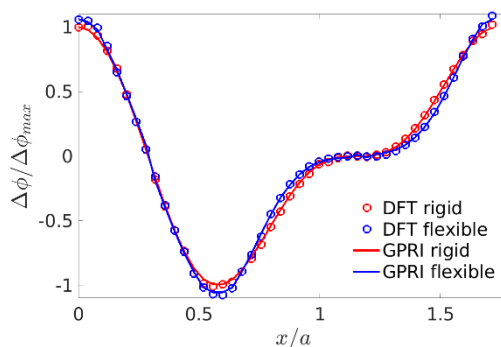

Figure S1. Polarization profiles calculated using DFT (open circles) and the $GPRI^{h-BN}$ (full lines) for rigid (red) and vertically relaxed (blue) shifts along the armchair direction. The x-axis is normalized to the intralayer lattice constant of h-BN $\left(a = 2.51\text{Å}\right)$.

1.3 Unnormalized polarization profiles

In Fig. 1b of the main text we show the normalized DFT polarization profile calculated by the method described in section 1.1. For completeness, in Fig. S2 we present the reference DFT curve (blue) without normalization for bilayer h-BN. Furthermore, in Fig. 3b, Fig. 4b, and Fig. 4f of the main text we presented potential drop calculations performed for a set of nudged elastic band (NEB)[12] intermediate image configurations between the high symmetry stacking modes along the sliding path of a few transition metal dichalcogenide interfaces. While this was not required for h-BN, for completeness we present in Fig. S2 a polarization profile calculated for a set of h-BN NEB images (red curve) connecting between the AB and BA stacking configurations (see Fig. 1a). These calculations were performed using the Vienna Ab-initio Simulation Package (VASP)[13] with the PBE generalized-gradient exchange-correlation density functional approximation[3] augmented by the Grimme-D3 dispersion correction with Becke-Johnson (BJ)[4, 5] damping.

The core electrons of the metal and chalcogen atoms were treated via the scalar-relativistic PAW approach. The plane wave energy cutoff was taken to be 850 eV and a k mesh of 12×12×1 points was used. A vertical vacuum size of 10 nm was set to avoid interactions between adjacent bilayer images. The atomic positions of the NEB images were relaxed with a force threshold of 1×10^{-3} eV/Å. To evaluate the vertical polarization, single point calculations were performed on the minimized NEB images, employing the dipole moment correction.
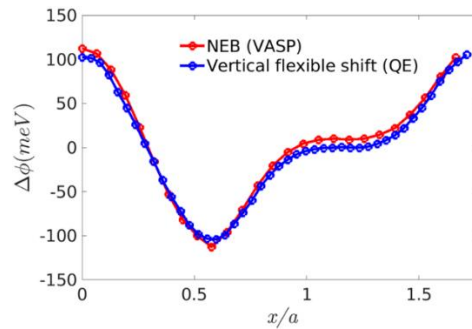
Figure S2. DFT polarization profiles for vertically relaxed shifts (blue curve) and NEB images (red curve) along the armchair direction for parallelly stacked bilayer h-BN. The x-axis is normalized to the intralayer lattice constant of h-BN $\left(a = 2.51\text{Å}\right)$.

1.4 Two-dimensional global polarization registry index

In Fig. 1d of the main text we presented the normalized two-dimensional (2D) DFT potential drop landscapes. For completeness, in Fig. S3 we present the corresponding unnormalized 2D DFT polarization landscape (Fig. S3a) and the difference between $GPRI^{h-BN}$ landscape and the normalized DFT data (Fig. S3b). The latter demonstrates that the maximal differences are lower than 10%.
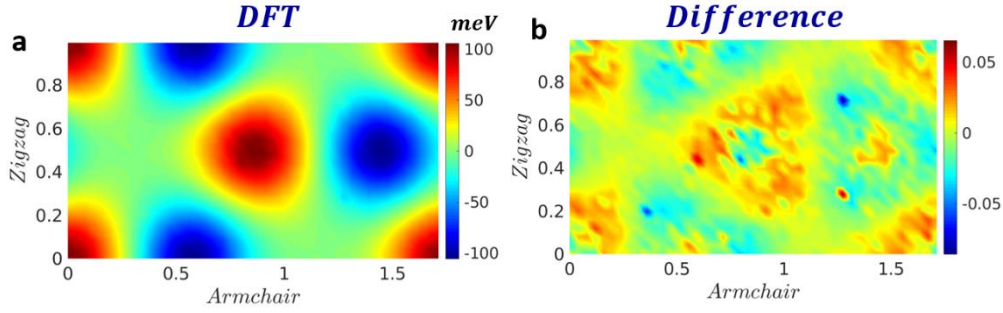
Figure S3. (a) Two-dimensional DFT polarization landscape without normalization and (b) the difference between the $GPRI^{h-BN}$ landscape and the normalized DFT data presented in Fig. 1d of the main text. The axes are normalized by the intralayer lattice constant of h-BN $(a = 2.51\text{Å})$. Color bars appear to the right of each panel.

1.5 Structural relaxation for local polarization registry index

In the main text, we presented a local polarization registry index ($LPRI^{h-BN}$) analysis of surface reconstruction in twisted h-BN bilayer. To this end, a 0.5° twisted AB stacked h-BN bilayer was generated using the LAMMPS package[14] with lateral periodic boundary conditions. In the vertical direction a sufficiently large vacuum size of 10 nm was applied to avoid spurious interactions between adjacent bilayer images. Intralayer and interlayer interactions were described via the Tersoff[15] intralayer potential and the dedicated registry dependent interlayer potential (ILP),[16, 17] respectively. We first optimized the geometry of the top layer atoms with fixed supercell size using the Fire algorithm[18] with a force tolerance of 10^{-4} eV/Å while fixing the positions of the bottom layer atoms to mimic the effect of a rigid substrate. This was followed by optimization of the supercell dimensions using the conjugate gradient (CG) algorithm[19] with a force tolerance of 10^{-3} eV/Å while scaling the rigid bottom layer according to the simulation box size. This approach is the same as the one recently used in a previous study.[20]

2. Interlayer Polarization Registry Index of homogeneous 2H TMD bilayers

2.1 Density functional theory computational details

The out-of-plane polarization of homogeneous 2H TMD bilayers (MoS$_2$, MoSe$_2$, WS$_2$, and WSe$_2$) at various stacking modes was calculated at the same level of theory presented in section 1.1 for h-BN bilayer, for which the scalar-relativistic PAW pseudopotentials were used. The coordinates of the AB stacked TMD bilayers are given at the end of this supplementary document. Table S2 summarizes the intralayer lattice constants (a), the interlayer distances (h_0, defined as the vertical distance between neighboring chalcogen atom in the adjacent layers), and the calculated potential drops of the relaxed AB stacked homogeneous 2H TMD bilayers. Our results are in good agreement with those calculated in Ref. 21 and are generally somewhat higher than the computational values reported in Ref. 11. The latter can be attributed to the differences in the interlayer distances, that were taken as their bulk values in Ref. 11, whereas herein they have been optimized. As may be expected[22], the experimental values are found to be consistently lower than the calculated values, probably due to the limitations of the local potential measurements under external bias and screening effects due to contaminants accumulating atop the surface.

Table S2. DFT structural parameters and potential drops of the various AB stacked homogeneous TMD bilayers. For comparison, previously reported experimental and computational potential drops are provided.

System	a (Å)	h_0 (Å)	$\Delta\phi$ (meV)			
			This work	Theory[21]	Theory[11]	Experiment[11]
MoS$_2$	3.156	2.95	76	69	64	47
MoSe$_2$	3.284	3.06	75	67	66	57
WS$_2$	3.157	2.97	62	63	66	56
WSe$_2$	3.287	3.10	65	66	56	56

Similar to section 1.1 for h-BN bilayer, HSE level of calculations were performed to support the results. The details of the calculations, other than the density functional approximation, were the same as those used in the PBE calculations. For example, for AB stacked WSe$_2$ bilayer, the potential drop obtained using HSE is 70 meV, compared to 65 meV by PBE. The abovementioned calculations (at both the PBE and HSE levels of theory) were performed using scalar-relativistic PAW pseudopotentials. To evaluate the effect of the scalar-relativistic approximation on the calculated potential drop, we repeated the calculations for AB stacked WSe$_2$ bilayer using full relativistic PAW pseudopotentials including spin-orbit interaction yielding a potential drop value of 71 meV, in excellent agreement with the scalar-relativistic result.

2.2 Global polarization registry index parameterization

The global polarization registry index for homogeneous $2H$ TMD bilayers ($GPRI^{2H-TMD}$) is the same as that described in SI section 1.2 above for h-BN bilayer. Table S3 presents the corresponding Gaussian widths, the average differences between the reference DFT values and the $GPRI^{2H-TMD}$ results obtained using the optimal parameter set, and the corresponding standard deviation.

Table S3. Fitted $GPRI^{2H-TMD}$ parameters for several homogeneous TMD bilayers. The effective Gaussian width of each atomic pair appearing in the table is given in units of $a/\sqrt{3}$, where a is the corresponding lattice constant (see Table S2). Average ($\bar{x}$) difference between the normalized reference DFT potential drop profile and the $GPRI^{2H-TMD}$ results and the corresponding standard deviation (σ) obtained using the optimal parameter sets are provided.

MoS$_2$	Parameter	WS$_2$	Parameter
$\sigma_{Mo}^{S}(\sigma_{S}^{Mo})$	0.15	$\sigma_{W}^{S}(\sigma_{S}^{W})$	0.19
$\bar{x}$	0.028	$\bar{x}$	0.051
σ	0.022	σ	0.033
MoSe$_2$	Parameter	WSe$_2$	Parameter
$\sigma_{Mo}^{Se}(\sigma_{Se}^{Mo})$	0.15	$\sigma_{W}^{Se}(\sigma_{Se}^{W})$	0.17
$\bar{x}$	0.024	$\bar{x}$	0.045
σ	0.024	σ	0.041

In Fig. 2b of the main text, the $GPRI^{2H-MoS2}$ results are compared to the reference DFT data. For completeness, we present in Fig. S4 the reference DFT polarization curves and the corresponding optimal $GPRI^{2H-TMD}$ profiles for the other three TMD bilayers considered. For each figure, the x-axis is normalized to the intralayer lattice constant of the corresponding TMD (see Table S2), and the DFT curve is normalized by the potential drop calculated for the AB stacked bilayer (see Table S2).

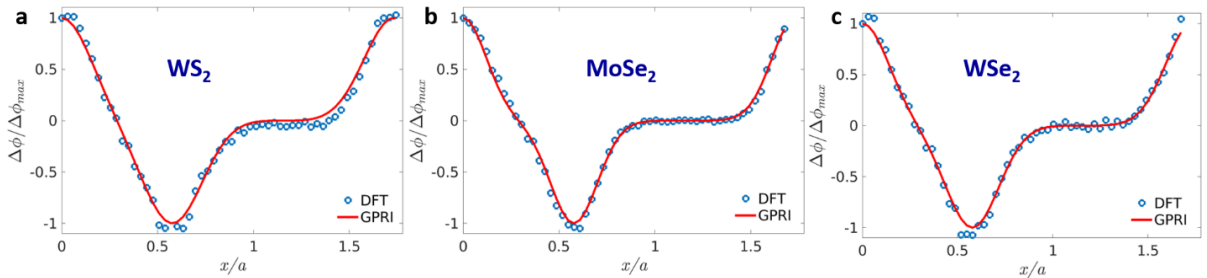**Figure S4.** Polarization profiles of parallelly stacked homogeneous (a) WS$_2$, (b) MoSe$_2$, and (c) WSe$_2$ bilayers calculated using DFT (blue open circles) and the $GPRI^{2H-WS_2}$ (full red line) for vertically relaxed shifts along the armchair direction.

2.3 Comparison between vertically relaxed and nudged elastic band MoS_2 polarization profiles

In Figs. 3b, 4b and 4f of the main text we presented polarization results of images along a nudged elastic band chain connecting the high symmetry stacking modes along the sliding path of a $1T'\,WTe_2$ bilayer and the heterojunctions of WS_2/MoS_2 and $MoSe_2/WS_2$, respectively. The corresponding results for MoS_2 (Fig. 2 of the main text) have been obtained via vertically relaxed shifts calculations. For completeness, in Fig. S5 we compare the MoS_2 vertically relaxed shifts polarization calculations (blue line) to nudged elastic band results (red). The level of theory used in these calculations was the same as that described in SI section 1.3 above for *h*-BN bilayer with a plane wave energy cutoff of 600 eV. The good agreement between the two polarization profiles justifies our use of the nudged elastic band approach for the other bilayer systems considered.
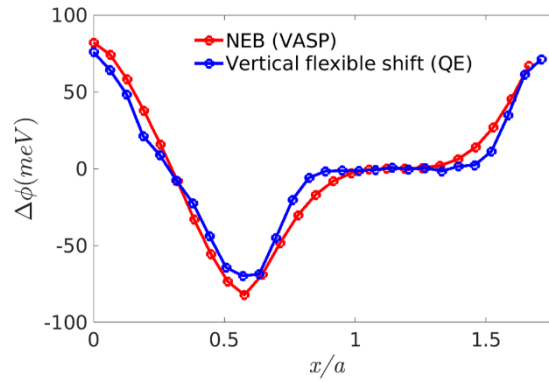
Figure S5. DFT polarization profiles for vertically relaxed shifts (blue curve, calculated by QE) and NEB images (red curve, calculated by VASP) along the armchair direction for parallelly stacked bilayer MoS_2. The *x*-axis is normalized to the intralayer lattice constant of MoS_2 $\left(a_{MoS_2} = 3.156\,\text{Å}\right)$.

2.4 Unnormalized polarization profiles

For the parameterization of the polarization registry index we presented in Fig. 2b of the main text normalized DFT polarization profiles of the various systems considered. For completeness, we present in Fig. S6 the original (unnormalized) DFT curves.
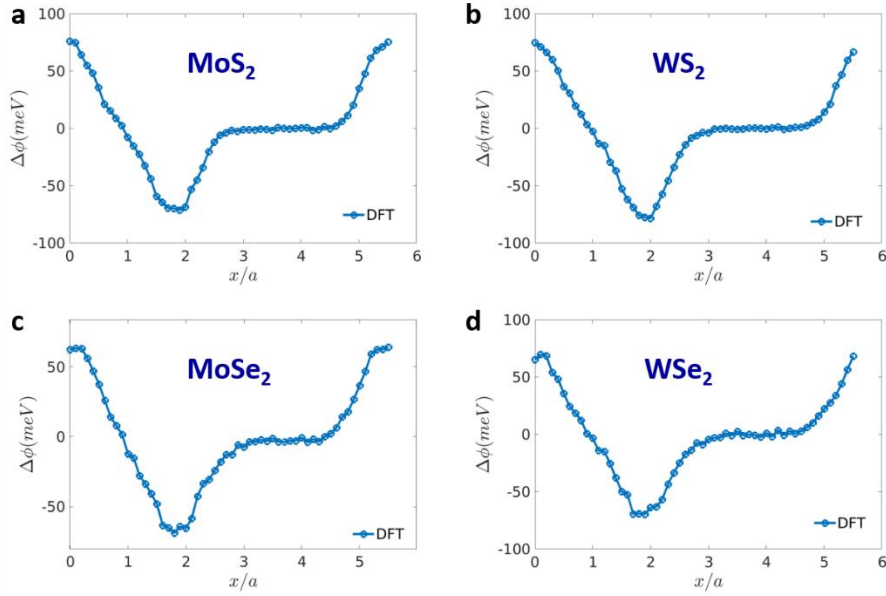
Figure S6. DFT polarization profiles for homogeneous (a) MoS₂, (b) WS₂, (c) MoSe₂, and (d) WSe₂ bilayers. The *x*-axis of each panel is normalized to the intralayer lattice constant of the corresponding TMD (see Table S2).

2.5 Two-dimensional global polarization registry index

In Fig. 2d of the main text we present a comparison between the normalized two-dimensional DFT potential drop map of MoS₂ bilayer and the corresponding $GPRI^{2H-MoS_2}$ landscape. For completeness, in Fig. S7 we present the unnormalized DFT results and the difference between the normalized DFT and $GPRI^{2H-MoS_2}$ maps. The latter demonstrates that the maximal differences are lower than 10%.

Figure S7. (a) Two-dimensional DFT polarization landscape without normalization and (b) the difference between the $GPRI^{2H-MoS_2}$ landscape and the normalized DFT data presented in Fig. 2d of the main text. The axes are normalized by the intralayer lattice constant of MoS₂ $\left(a_{MoS_2} = 3.156\,\text{Å}\right)$. Color bars appear to the right of each panel.

2.6 Structural relaxation for local polarization registry index

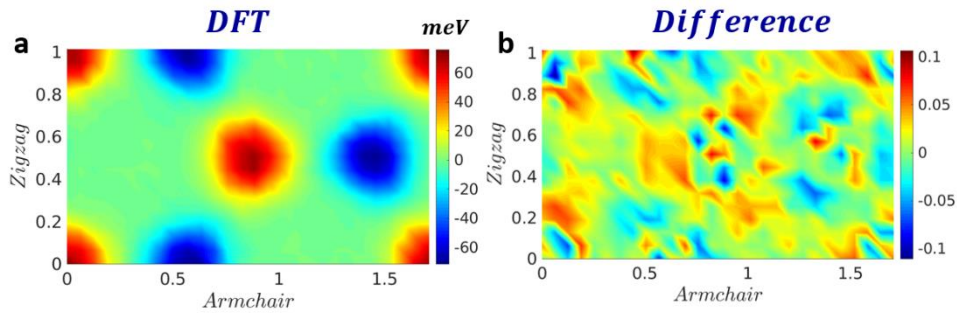In the main text, we presented a local polarization registry index ($LPRI^{2H-MoS_2}$) analysis of surface reconstruction in twisted MoS$_2$ bilayer. To this end, a 0.5° twisted AB stacked MoS_2 bilayer was generated using the LAMMPS[14] package. Periodic boundary conditions were applied in the lateral directions. In the vertical direction a sufficiently large vacuum size of 10 nm was applied to avoid spurious interactions between adjacent bilayer images. The intralayer interactions were described via the second-generation reactive empirical bond order (REBO) potential,[23] and the interlayer interactions were calculated by a dedicated registry dependent interlayer potential.[24] The Fire algorithm with a force tolerance of 10^{-6} eV/Å was used to relax the structure (including the box size) keeping the lower sulfur atomic sublayer of the bottom MoS$_2$ layer fixed to mimic the effect of a rigid substrate.

3. Interlayer Polarization Registry Index of bilayer $1T'$-WTe$_2$

3.1 Density functional theory computational details

In the case of $1T' - WTe_2$ we found that using vertically relaxed structures along the sliding path results in an unsmooth polarization profile. Therefore, we resorted to nudged elastic band calculations to obtain intermediate interlayer configurations between the high symmetry stacking modes along the sliding path.[12] For the sliding along the x-direction, we chose the lowest energy stacking modes I and II, whose initial structures are given in Ref. 25 herein (the coordinates of stacking mode II are given at the end of this file, the corresponding coordinates of mode I can be obtained via a mirror reflection of those of mode II along the lateral plane), as our anchors and stretched the image bands between them along the positive and negative x sliding directions. For the sliding along the y-direction, we chose stacking modes II for both anchors and stretched the image bands along a full lattice period in the y-direction. The DFT level of theory is the same as that described in SI section 1.1 above for h-BN bilayer using a plane wave energy cutoff of 500 eV.

3.2 Global polarization registry index parameterization

The parameterization procedure of the global polarization registry index of $1T' - WTe_2$ bilayer ($GPRI^{1T'-WTe_2}$) is similar to that described in SI section 1.2 above for the h-BN bilayer. Here, however, to account for the different vertical distances between inequivalent W and Te atoms on adjacent layers, the projected overlaps are scaled by an exponential function, introducing the exponent, α, as an additional fitting parameter (see Eqs. (3) and (4) of the main text). Due to the lack of structural symmetry in the two lateral directions, the DFT polarization curves along the x- and y- sliding paths are fitted simultaneously. In Fig. 3b of the main text we compared the $GPRI^{1T'-WTe_2}$ and reference DFT polarization profiles along the x-direction. For completeness, we present a similar comparison along the y-direction in Fig. S8, showing good agreement between the $GPRI^{1T'-WTe_2}$ and the reference DFT results.

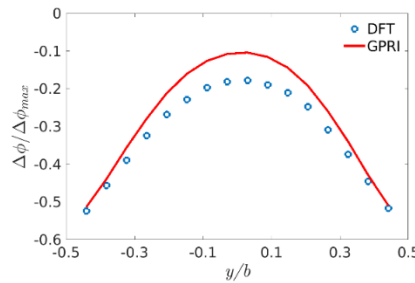**Figure S8.** $GPRI^{1T'-WTe_2}$ (full red line) and DFT (blue open circles) polarization profiles of $1T' - WTe_2$ shifted along the y-direction. The DFT curves are normalized by the potential drop calculated for stacking mode III ($\Delta\phi_{max} = 64\ meV$, see Fig, 3a of the main text). The x-axis values are normalized to the intralayer lattice constant of $1T'\ WTe_2$ along the y direction ($b = 3.47$ Å).

Table S4 presents the Gaussian widths, α, and the average differences between the reference DFT values and the $GPRI^{1T'-WTe_2}$ results obtained using the optimal parameter set and the corresponding standard deviation.

Table S4. Fitted $GPRI^{1T'-WTe_2}$ parameters for the $1T' - WTe_2$ bilayer. The Gaussian width of each atomic pair appearing in the table is given in units of a, where a is the intralayer lattice constant along the x direction $\left(a_{1T'-WTe_2} = 6.26\ \text{Å}\right)$. Average $(\bar{x})$ difference between the normalized reference DFT potential drop profile and the $GPRI^{1T'-WTe_2}$ results and the corresponding standard deviation (σ) obtained using the optimal parameter sets are provided.

1T'-WTe$_2$	Parameter
$\sigma_{W_1}^{Te_1}(\sigma_{Te_1}^{W_1})$	0.01
$\sigma_{W_1}^{Te_2}(\sigma_{Te_2}^{W_1})$	0.16
$\sigma_{W_2}^{Te_1}(\sigma_{Te_1}^{W_2})$	0.07
$\sigma_{W_2}^{Te_2}(\sigma_{Te_2}^{W_2})$	0.18
α (Å^{-1})	0.77
$\bar{x}$	0.030
σ	0.031

To explain the origin of the large differences seen in Table S4 between the Gaussian widths associated with Te_1 and Te_2 atomic positions, Bader[26] charge analysis was performed for stacking mode II (see Fig. 3a of the main text) of the $1T' - WTe_2$ bilayer. The atomic Bader charges appearing in Fig. S9 indeed associate a considerably lower effective charge to the Te_1 atomic positions as compared to their Te_2 counterparts, justifying the larger Gaussian width required for the latter in the $GPRI^{1T'-WTe_2}$ expression. Notably, all W positions bare similar Bader charges.

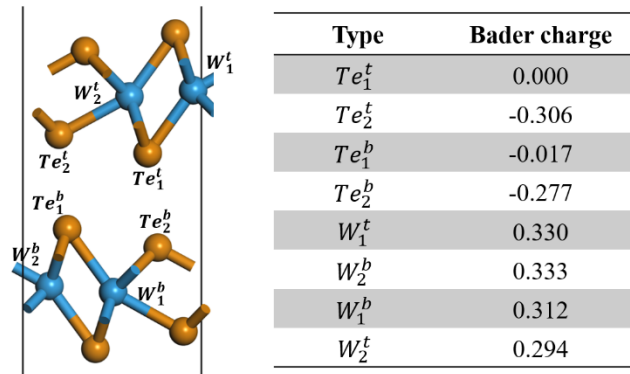| Type	Bader charge
Te_1^t	0.000
Te_2^t	-0.306
Te_1^b	-0.017
Te_2^b	-0.277
W_1^t	0.330
W_2^b	0.333
W_1^b	0.312
W_2^t	0.294

Figure S9. Bader charge analysis of a mode II stacked $1T' - WTe_2$ bilayer. Atomic labels are shown on the bilayer illustration. Top (bottom) layer atoms are marked with the label t(b).

3.3 Comparison between NEB and vertically flexible shifts polarization profiles

As discussed in the main text, for $1T' - WTe_2$ we found that vertically flexible shift calculations are insufficient to obtain smooth polarization profiles. Therefore, we resorted to nudged elastic band calculations (see Fig. 3b of the main text). To demonstrate this, in Fig. S10 we compare the polarization profiles (without normalization) obtained using vertically relaxed shifts (blue) and nudged elastic band calculations (red). The level of DFT theory in these calculations is the same as that used for the *h*-BN bilayer in section 1.1 above. Clearly, both curves show similar qualitative behavior with the nudged elastic band approach producing a much more regular curve.
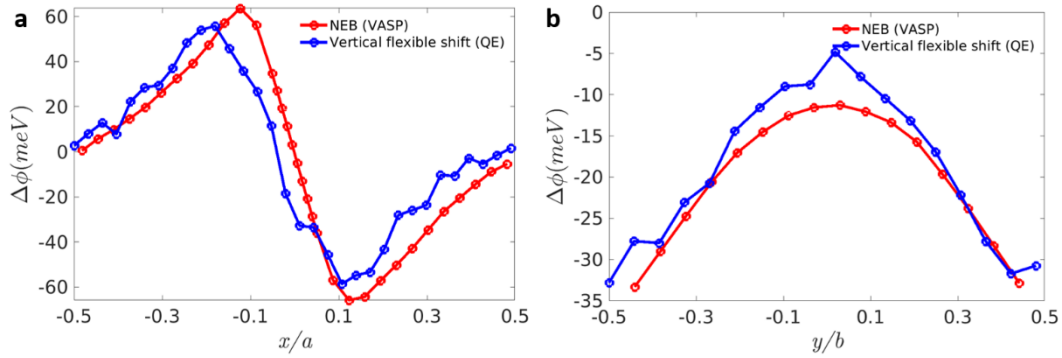
Figure S10. Bilayer $1T'\ WTe_2$ DFT polarization profiles along (a) the *x*- and (b) *y*-directions, obtained via vertically relaxed shift calculations (blue curve, calculated by QE) and the NEB approach (red curve, calculated by VASP).

3.4 The calculation of the local polarization registry index

The calculation of the local polarization registry index of a given atom in $1T' - WTe_2$ $\left(LPRI^{1T'-WTe_2}\right)$ relies on averaging the $GPRI^{1T'-WTe_2}$ values calculated for 4 atomic quartets (defining a unit cell within the layer) including the given atom and three of 10 of its intralayer neighbors. For example, the 10 neighbors considered in the calculation of the $LPRI^{1T'-WTe_2}$ of a Te atom are presented in Fig. S11, where the $LPRI^{1T'-WTe_2}$ is obtained by first evaluating the $GPRI^{1T'-WTe_2}$ for following atomic quartets $\{0\ 1\ 2\ 3\}$, $\{0\ 3\ 4\ 5\}$, $\{0\ 6\ 7\ 8\}$, $\{0\ 8\ 9\ 10\}$ (0 representing the given Te atom) and then averaging over the four results.
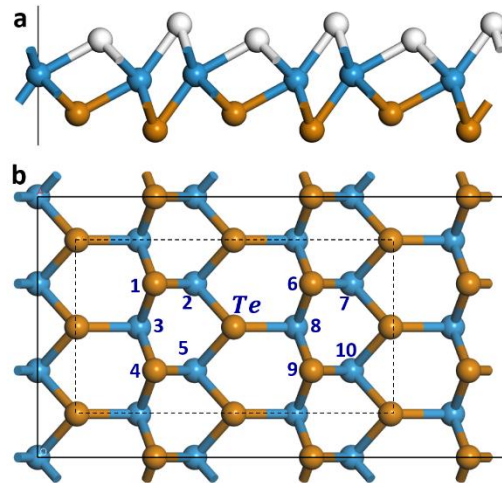
Figure S11. Side view (a) and top view (b) of an $1T' - WTe_2$ single layer containing 3×3 unit cells. The external Te sublayer atoms (marked in white in panel (a)) are not included in the $GPRI^{1T'-WTe_2}$ calculation of the bilayer. For clarity of the presentation, these atoms are omitted in panel (b). The dashed lines in panel (b) mark a 2×2 supercell. The 10 neighbors of the central Te atom used for the calculation of the $LPRI^{1T'-WTe_2}$ are labeled by the numbers 1-10.

4. Interlayer Registry of heterogeneous $2H$ TMD bilayers

4.1 Density functional theory computational details

The DFT polarization curves of heterogeneous bilayers formed between MoS_2, $MoSe_2$, WS_2, and WSe_2 were calculated at the same level of DFT theory described in SI section 1.1 above, with a plane wave energy cutoff of 600 eV. The calculations have been performed using NEB images, similar to those discussed in SI section 1.3 above. Specifically, we chose the lowest energy AB and BA stacking modes (see Fig. 4a, 4e) as our anchors and stretched the image bands between them along the positive and negative armchair directions. For the heterogeneous interfaces the lateral lattice vectors of the bilayer were chosen as the average of the corresponding lattice vectors of the relaxed individual layers, which are stretched or compressed accordingly to form the bilayer supercell. The coordinates of the AB stacked heterogenous bilayers are given at the end of this document.

Table S5 summarizes the structural parameters (lattice constants, a, and interlayer distances, h_0, determined by the vertical distance between neighboring chalcogen atom in the adjacent layers) and the potential drops obtained for the six relaxed heterogeneous bilayers considered.

Table S5. DFT structural parameters obtained for the various TMD heterogenous bilayers relaxed at their AB stacking mode and the corresponding potential drops across the bilayer calculated for the AB, and BA stacking modes.

System	a (Å)	h_0 (Å)	$\Delta\phi$ (meV)	
			AB	BA
WS_2/MoS_2	3.187	2.897	126	-36
$WSe_2/MoSe_2$	3.286	3.003	124	-23
$MoSe_2/MoS_2$	3.251	2.908	214	54
WSe_2/WS_2	3.252	2.942	168	12
WSe_2/MoS_2	3.252	2.913	247	88
$MoSe_2/WS_2$	3.252	2.942	135	-20

4.2 Global polarization registry index parameterization

The parameterization procedure of the global polarization registry index of heterogeneous TMD bilayers ($GPRI^{M_1X_1/M_2X_2}$) is similar to that described in SI section 1.2 above for the h-BN bilayer. Table S6 presents the corresponding Gaussian widths, the average differences between the reference DFT values and the $GPRI^{M_1X_1/M_2X_2}$ results obtained using the optimal parameter set, and the corresponding standard deviation.

Table S6. Fitted $GPRI^{M_1X_1/M_2X_2}$ parameters for several heterogeneous TMD bilayers. The effective Gaussian width of each atomic pair appearing in the table is given in units of $a/\sqrt{3}$, where a is the corresponding supercell lattice constant (see Table S5). Average $(\bar{x})$ difference between the normalized reference DFT potential drop profile and the $GPRI^{M_1X_1/M_2X_2}$ results and the corresponding standard deviation (σ) obtained using the optimal parameter sets are provided.

WS$_2$/MoS$_2$	Parameter	WSe$_2$/MoSe$_2$	Parameter
$\sigma_W^S(\sigma_S^W)$	0.22	$\sigma_W^{Se}(\sigma_{Se}^W)$	0.21
$\sigma_{Mo}^S(\sigma_S^{Mo})$	0.12	$\sigma_{Mo}^{Se}(\sigma_{Se}^{Mo})$	0.10
$\sigma_W^{Mo}(\sigma_{Mo}^W)$	0.18	$\sigma_W^{Mo}(\sigma_{Mo}^W)$	0.22
σ_S^S	0.16	σ_{Se}^{Se}	0.2
$\bar{x}$	0.025	$\bar{x}$	0.028
σ	0.029	σ	0.033
MoSe$_2$/MoS$_2$	**Parameter**	**WSe$_2$/WS$_2$**	**Parameter**
$\sigma_{Mo}^{Se}(\sigma_{Se}^{Mo})$	0.02	$\sigma_W^{Se}(\sigma_{Se}^W)$	0.07
$\sigma_{Mo}^S(\sigma_S^{Mo})$	0.32	$\sigma_W^S(\sigma_S^W)$	0.28
σ_{Mo}^{Mo}	0.08	σ_W^W	0.13
$\sigma_S^{Se}(\sigma_{Se}^S)$	0.06	$\sigma_S^{Se}(\sigma_{Se}^S)$	0.10
$\bar{x}$	0.042	$\bar{x}$	0.039
σ	0.056	σ	0.047
WSe$_2$/MoS$_2$	**Parameter**	**MoSe$_2$/WS$_2$**	**Parameter**
$\sigma_{Mo}^{Se}(\sigma_{Se}^{Mo})$	0.01	$\sigma_W^{Se}(\sigma_{Se}^W)$	0.10
$\sigma_W^S(\sigma_S^W)$	0.34	$\sigma_{Mo}^S(\sigma_S^{Mo})$	0.23
$\sigma_W^{Mo}(\sigma_{Mo}^W)$	0.21	$\sigma_W^{Mo}(\sigma_{Mo}^W)$	0.17
$\sigma_S^{Se}(\sigma_{Se}^S)$	0.19	$\sigma_S^{Se}(\sigma_{Se}^S)$	0.19
$\bar{x}$	0.046	$\bar{x}$	0.031
σ	0.055	σ	0.032

In Fig. 4b and 4f of the main text we compared the DFT polarization curves of WS_2/MoS_2 and $MoSe_2/WS_2$ heterogeneous bilayers to the corresponding $GPRI^{WS_2/MoS_2}$ and $GPRI^{MoSe_2/WS_2}$ profiles. For completeness, we present in Fig. S12 below the comparison for the other four heterogeneous bilayer models considered. The x-axis of each panel is normalized to the intralayer lattice constant of the corresponding model (see Table S5), and the DFT curve is normalized by the potential drop calculated for the corresponding AB stacked bilayer (see Table S5).
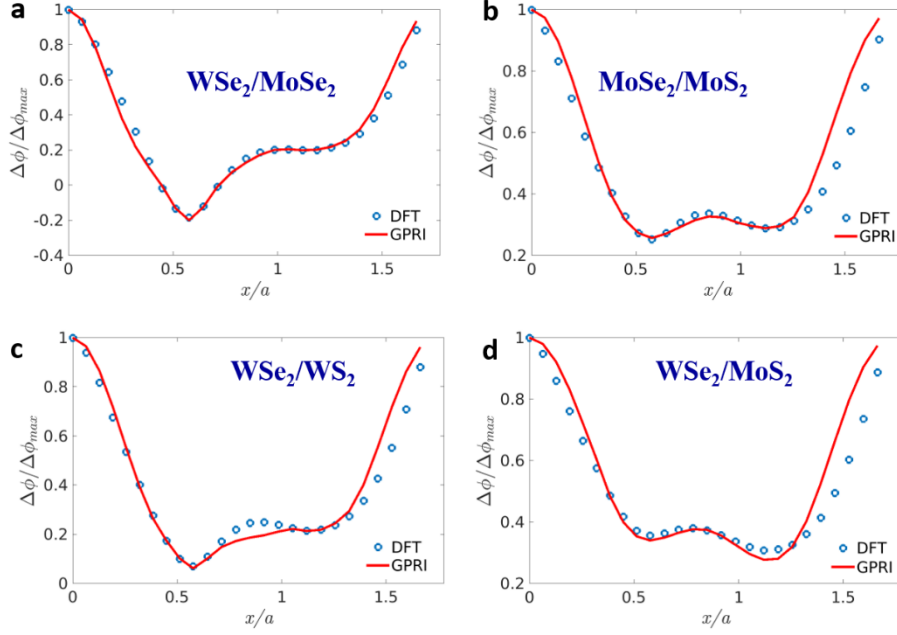
Figure S12. Polarization profiles of parallelly stacked (a) $WSe_2/MoSe_2$ (b) $MoSe_2/MoS_2$ (c) WSe_2/WS_2, and (d) WSe_2/MoS_2 heterogeneous TMD bilayers calculated using DFT (blue open circles) and the $GPRI^{M_1X_1/M_2X_2}$ (full red lines) along the armchair direction.

4.3 Comparison between NEB and vertically flexible shifts polarization profiles

As discussed in the main text, for the WS_2/MoS_2 and $MoSe_2/WS_2$ heterogeneous interfaces we found that vertically flexible shift calculations are insufficient to obtain smooth polarization profiles. Therefore, we resorted to nudged elastic band calculations (see Figs. 4b and 4f of the main text). To demonstrate this, in Fig. S13 we compare the polarization profiles (without normalization) obtained using vertically relaxed shifts (blue) and nudged elastic band calculations (red). The level of DFT theory in these calculations is the same as that used for the h-BN bilayer in section 1.1 above. Clearly, both curves show similar qualitative behavior with the nudged elastic band approach producing a much more regular curve.
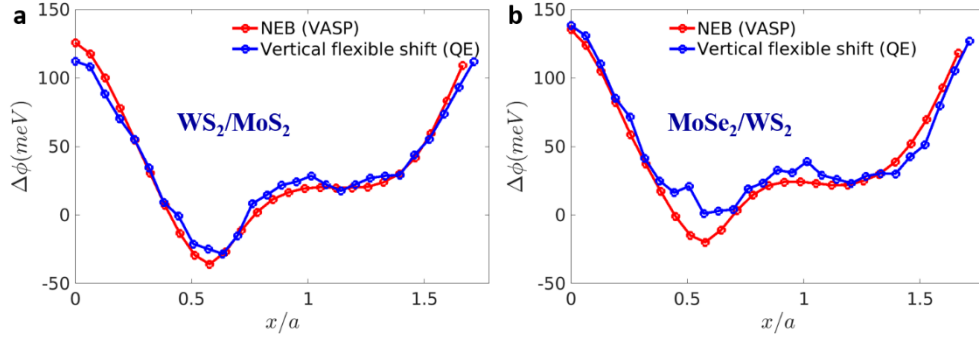
Figure S13. DFT polarization profiles along the x sliding direction of the (a) WS_2/MoS_2 and (b) $MoSe_2/WS_2$ heterogeneous interfaces, obtained via vertically relaxed shift calculations (blue curve, calculated by QE) and the NEB approach (red curve, calculated by VASP).

4.4 Unnormalized polarization profiles

In Figs. 4b and 4f of the main text we show the normalized DFT polarization profile calculated by the method described in section 1.1. For completeness, in Fig. S14 we present the reference DFT curve (blue) without normalization for all the six heterogeneous bilayers considered. In each panel, the x-axis is normalized to the intralayer lattice constant of the corresponding bilayer model (see Table S5).
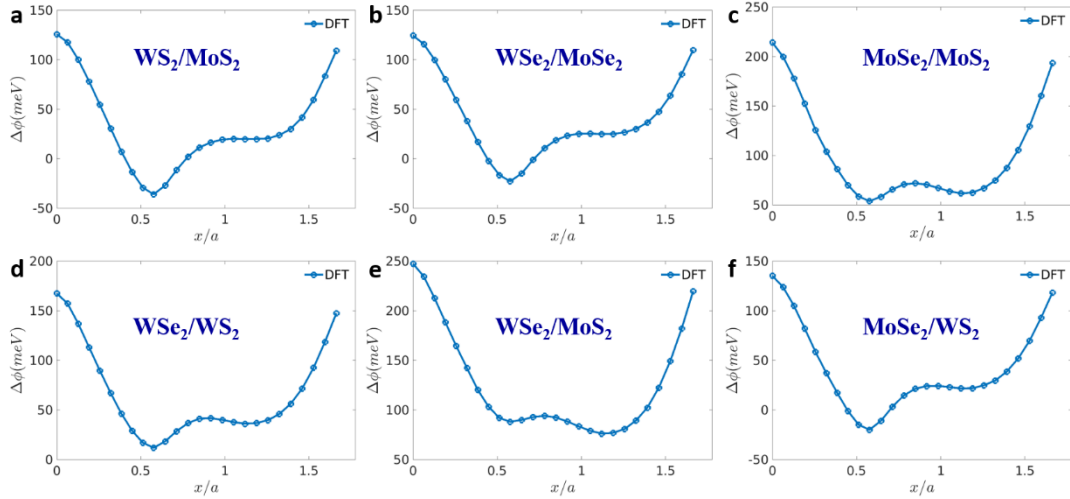

Figure S14. DFT polarization profiles without normalization for the heterogenous bilayers of (a) WS_2/MoS_2, (b) $WSe_2/MoSe_2$, (c) $MoSe_2/MoS_2$, (d) WSe_2/WS_2, (e) WSe_2/MoS_2, and (f) $MoSe_2/WS_2$. In each panel, the x-axis is normalized to the intralayer lattice constant of the corresponding bilayer model system (see Table S5).

4.5 Structural relaxation for local polarization registry index analysis

In Fig. 4c and 4g of the main text, we presented a local polarization registry index ($LPRI^{WS_2/MoS_2}$ and $LPRI^{MoSe_2/WS_2}$) analysis of surface reconstruction in twisted WS_2/MoS_2 and $MoSe_2/WS_2$ heterogeneous bilayers. Since WS_2 and MoS_2 have practically the same intralayer lattice vectors, we generated, using the LAMMPS[14] package, a $0.5°$ twisted AB stacked WS_2/MoS_2 bilayer, where surface reconstruction is apparent. On the contrary, $MoSe_2$ and WS_2 have an intrinsic ~4% intralayer lattice mismatch. Hence, surface reconstruction is obtained already for the aligned unstressed parallelly stacked bilayer interface, which we generated. Periodic boundary conditions were applied in the lateral directions and in the vertical direction a sufficiently large vacuum size of 10 nm was applied to avoid spurious interactions between adjacent bilayer images. The intralayer interactions were described via the Stillinger–Weber (SW) potential[27], and the interlayer interactions were calculated using a recently parameterized Kolmogorov–Crespi type potential.[28] The Fire algorithm[18] was used with a force tolerance of 10^{-6} eV/Å to relax the structure (including the box dimensions) keeping the lower atomic sublayer of the bottom layer fixed to mimic a rigid substrate.

References:

1. Fletcher, R., *Practical Methods of Optimization*. John Wiley & Sons: 2013.

2. Giannozzi, P.; Baroni, S.; Bonini, N.; Calandra, M.; Car, R.; Cavazzoni, C.; Ceresoli, D.; Chiarotti, G. L.; Cococcioni, M.; Dabo, I.; Dal Corso, A.; de Gironcoli, S.; Fabris, S.; Fratesi, G.; Gebauer, R.; Gerstmann, U.; Gougoussis, C.; Kokalj, A.; Lazzeri, M.; Martin-Samos, L.; Marzari, N.; Mauri, F.; Mazzarello, R.; Paolini, S.; Pasquarello, A.; Paulatto, L.; Sbraccia, C.; Scandolo, S.; Sclauzero, G.; Seitsonen, A. P.; Smogunov, A.; Umari, P.; Wentzcovitch, R. M., Quantum Espresso: A Modular and Open-Source Software Project for Quantum Simulations of Materials. *Journal of Physics: Condensed Matter* **2009,** 21, (39), 395502.

3. Perdew, J. P.; Burke, K.; Ernzerhof, M., Generalized Gradient Approximation Made Simple. *Physical Review Letters* **1996,** 77, (18), 3865-3868.

4. Grimme, S.; Antony, J.; Ehrlich, S.; Krieg, H., A Consistent and Accurate Ab Initio Parametrization of Density Functional Dispersion Correction (DFT-D) for the 94 Elements H-Pu. *The Journal of Chemical Physics* **2010,** 132, (15), 154104.

5. Grimme, S.; Ehrlich, S.; Goerigk, L., Effect of the Damping Function in Dispersion Corrected Density Functional Theory. *Journal of Computational Chemistry* **2011,** 32, (7), 1456-1465.

6. Monkhorst, H. J.; Pack, J. D., Special Points for Brillouin-Zone Integrations. *Physical Review B* **1976,** 13, (12), 5188-5192.

7. Heyd, J.; Scuseria, G. E., Efficient Hybrid Density Functional Calculations in Solids: Assessment of the Heyd–Scuseria–Ernzerhof Screened Coulomb Hybrid Functional. *The Journal of Chemical Physics* **2004,** 121, (3), 1187-1192.

8. Heyd, J.; Scuseria, G. E., Assessment and Validation of a Screened Coulomb Hybrid Density Functional. *The Journal of Chemical Physics* **2004,** 120, (16), 7274-7280.

9. Heyd, J.; Scuseria, G. E.; Ernzerhof, M., Hybrid Functionals Based on a Screened Coulomb Potential. *The Journal of Chemical Physics* **2003,** 118, (18), 8207-8215.

10. Heyd, J.; Scuseria, G. E.; Ernzerhof, M., Erratum: "Hybrid Functionals Based on a Screened Coulomb Potential" [J. Chem. Phys. 118, 8207 (2003)]. *The Journal of Chemical Physics* **2006,** 124, (21), 219906.

11. Wang, X.; Yasuda, K.; Zhang, Y.; Liu, S.; Watanabe, K.; Taniguchi, T.; Hone, J.; Fu, L.; Jarillo-Herrero, P., Interfacial Ferroelectricity in Rhombohedral-Stacked Bilayer Transition Metal Dichalcogenides. *Nat Nanotechnol* **2022,** 17, (4), 367-371.

12. Henkelman, G.; Uberuaga, B. P.; Jónsson, H., A Climbing Image Nudged Elastic Band Method for Finding Saddle Points and Minimum Energy Paths. *The Journal of Chemical Physics* **2000,** 113, (22), 9901-9904.

13. Kresse, G.; Furthmuller, J., Efficient Iterative Schemes for Ab Initio Total-Energy Calculations Using a Plane-Wave Basis Set. *Physical Review B* **1996,** 54, (16), 11169-11186.

14. Plimpton, S., Fast Parallel Algorithms for Short-Range Molecular Dynamics. *Journal of Computational Physics* **1995,** 117, (1), 1-19.

15. Sevik, C.; Kinaci, A.; Haskins, J. B.; Cagin, T., Characterization of Thermal Transport in Low-Dimensional Boron Nitride Nanostructures. *Physical Review B* **2011,** 84, (8), 085409.

16. Leven, I.; Azuri, I.; Kronik, L.; Hod, O., Inter-Layer Potential for Hexagonal Boron Nitride. *Journal of Chemical Physics* **2014,** 140, (10), 104106.

17. Maaravi, T.; Leven, I.; Azuri, I.; Kronik, L.; Hod, O., Interlayer Potential for Homogeneous Graphene and Hexagonal Boron Nitride Systems: Reparametrization for Many-Body Dispersion Effects. *Journal of Physical Chemistry C* **2017,** 121, (41), 22826-22835.

18. Sheppard, D.; Terrell, R.; Henkelman, G., Optimization Methods for Finding Minimum Energy Paths. *The Journal of Chemical Physics* **2008,** 128, (13), 134106.

19. Bitzek, E.; Koskinen, P.; Gähler, F.; Moseler, M.; Gumbsch, P., Structural Relaxation Made Simple. *Physical Review Letters* **2006,** 97, (17), 170201.

20. Vizner Stern, M.; Waschitz, Y.; Cao, W.; Nevo, I.; Watanabe, K.; Taniguchi, T.; Sela, E.;

Urbakh, M.; Hod, O.; Ben Shalom, M., Interfacial Ferroelectricity by Van Der Waals Sliding. *Science* **2021,** 372, (6549), 1462-1466.

21. Ferreira, F.; Enaldiev, V. V.; Fal'ko, V. I.; Magorrian, S. J., Weak Ferroelectric Charge Transfer in Layer-Asymmetric Bilayers of 2D Semiconductors. *Scientific Reports* **2021,** 11, (1), 13422.

22. Deb, S.; Cao, W.; Raab, N.; Watanabe, K.; Taniguchi, T.; Goldstein, M.; Kronik, L.; Urbakh, M.; Hod, O.; Shalom, M. B., Cumulative Polarization in Conductive Interfacial Ferroelectrics. Nature 2022. DOI: 10.1038/s41586-022-05341-5.

23. Liang, T.; Phillpot, S. R.; Sinnott, S. B., Erratum: Parametrization of a Reactive Many-Body Potential for Mo--S Systems [Phys. Rev. B 79, 245110 (2009)]. *Physical Review B* **2012,** 85, (19), 199903.

24. Ouyang, W.; Sofer, R.; Gao, X.; Hermann, J.; Tkatchenko, A.; Kronik, L.; Urbakh, M.; Hod, O., Anisotropic Interlayer Force Field for Transition Metal Dichalcogenides: The Case of Molybdenum Disulfide. *J Chem Theory Comput* **2021,** 17, (11), 7237-7245.

25. Yang, Q.; Wu, M.; Li, J., Origin of Two-Dimensional Vertical Ferroelectricity in WTe_2 Bilayer and Multilayer. *The Journal of Physical Chemistry Letters* **2018,** 9, (24), 7160-7164.

26. Tang, W.; Sanville, E.; Henkelman, G., A Grid-Based Bader Analysis Algorithm without Lattice Bias. *Journal of Physics-Condensed Matter* **2009,** 21, (8), 084204.

27. Jiang, J.-W., Misfit Strain-Induced Buckling for Transition-Metal Dichalcogenide Lateral Heterostructures: A Molecular Dynamics Study. *Acta Mechanica Solida Sinica* **2019,** 32, (1), 17-28.

28. Naik, M. H.; Maity, I.; Maiti, P. K.; Jain, M., Kolmogorov–Crespi Potential for Multilayer Transition-Metal Dichalcogenides: Capturing Structural Transformations in Moiré Superlattices. *The Journal of Physical Chemistry C* **2019,** 123, (15), 9770-9778.

Coordinates of typical high symmetry stacking modes of the studied systems

1. AB stacked h-BN bilayer.

#lattice vectors (angstrom)

  2.510628370   0.000000002   0.000000000

 -1.255314683   2.174268292   0.000000000

  0.000000000   0.000000000 100.000000000

#coordinates, x, y, z (angstrom)

B	0.0000000003	1.4495129197	48.3247041885
B	1.2553152743	0.7247553736	51.6749704473
N	1.2553146837	0.7247553736	48.3238024374
N	2.5106283700	0.0000000005	51.6765229269

2. AB stacked MoS_2 bilayer.

#lattice vectors (angstrom)

  3.155546256 -0.000000000   0.000000000

 -1.577773128   2.732783219   0.000000000

  0.000000000   0.000000000 100.000000000

#coordinates, x, y, z (angstrom)

Mo	-0.0000000019	1.8218554863	46.9621226257
Mo	1.5777732418	0.9109277422	53.0384762961
S	1.5777732418	0.9109277422	48.5269433744
S	3.1555462557	0.0000000000	54.6058888545
S	1.5777732418	0.9109277422	45.3939300565
S	3.1555462557	0.0000000000	51.4726387828

3. Stacking mode II of $1T' - WTe_2$ bilayer.

#lattice vectors (angstrom)

  3.4678156241037703   0.0000000000000000   0.0000000000000000

  0.0000000000000000   6.2594374611544925   0.0000000000000000

  0.0000000000000000   0.0000000000000000 111.0628404694354856

#coordinates, x, y, z (angstrom)

Te	0.0000000000000000	5.6275511620364318	50.6119721911902403
Te	0.0000000000000000	4.3750842016263460	56.8633773144354961
Te	1.7339078120518852	1.2670529173689027	57.5126033284901581
Te	1.7339078120518852	2.5416023901916431	50.0000000000000000

Te	1.7339078120518852	5.3440858591078406	61.0628404694354856
Te	1.7339078120518852	4.7257387913241642	53.5513980140315482
Te	0.0000000000000000	1.5523872431109862	54.1979244499327422
Te	0.0000000000000000	2.1773177475295609	60.4504060033088848
W	0.0000000000000000	5.9687468627887768	59.0737371497863109
W	0.0000000000000000	3.1632668375055228	51.9912153327301709
W	1.7339078120518852	0.9308084726492641	52.2032805484601425
W	1.7339078120518852	3.7361040556833243	58.8553067785679502

4. AB stacked WS_2/MoS_2 bilayer.

#lattice vectors (angstrom)

3.1869612949999997	0.0000000000000000	0.0000000000000000
-1.5934806474999998	2.7599894423477522	0.0000000000000000
0.000000000000063	0.000000000000109	100.0000000000000000

#coordinates, x, y, z (angstrom)

W	1.5934806475000032	0.9199964807825768	52.9998502644904477
Mo	-0.0000000000000084	1.8399929615651667	46.9881569456243824
S	3.1869612949999997	0.0000000000000000	54.5656789693687898
S	3.1869612949999997	0.0000000000000000	51.4363334198148365
S	1.5934806475000030	0.9199964807825763	48.5398442757292514
S	1.5934806475000027	0.9199964807825760	45.4323775491066897

5. AB stacked $MoSe_2/WS_2$ bilayer.

#lattice vectors (angstrom)

3.2514895350000002	0.0000000000000000	0.0000000000000000
-1.6257447675000001	2.8158725374492515	0.0000000000000000
0.0000000000000000	0.0000000000000000	100.000000000000000

#coordinates, x, y, z (angstrom)

Mo	1.6257447674999885	0.9386241791497572	53.0782399021381011
W	0.0000000000000115	1.8772483582994943	46.9096955477169004
Se	3.2514895350000002	0.0000000000000000	54.7656701075482886
Se	3.2514895350000002	0.0000000000000000	51.3924568990014450
S	1.6257447674999885	0.9386241791497572	48.4506997807832605
S	1.6257447674999885	0.9386241791497572	45.3654791869464589